MOLECULAR IMAGING AND BIOLOGY

Mol Imaging Biol (2019) 21:86–94
DOI: 10.1007/s11307-018-1199-6

Published Online: 10 May 2018

RESEARCH ARTICLE

Androgen Receptor Signaling in Castration-Resistant Prostate Cancer Alters Hyperpolarized Pyruvate to Lactate Conversion and Lactate Levels *In Vivo*

Niki Zacharias,[1,2,3] Jaehyuk Lee,[1] Sumankalai Ramachandran,[4] Sriram Shanmugavelandy,[1] James McHenry,[1] Prasanta Dutta,[1] Steven Millward,[1] Seth Gammon,[1] Eleni Efstathiou,[4] Patricia Troncoso,[5] Daniel E. Frigo,[1,4] David Piwnica-Worms,[1] Christopher J Logothetis,[4,6] Sankar N Maity,[4] Mark A Titus,[4] Pratip Bhattacharya[1]

[1]*Department of Cancer Systems Imaging, The University of Texas MD Anderson Cancer Center, 1881 East Road, Unit 1907, Houston, TX, 77054, USA*
[2]*Department of Bioengineering, Rice University, Houston, TX, USA*
[3]*Department of Urology, The University of Texas MD Anderson Cancer Center, Houston, TX, USA*
[4]*Department of Genitourinary Medical Oncology, The University of Texas MD Anderson Cancer Center, Houston, TX, USA*
[5]*Department of Pathology, The University of Texas M.D. Anderson Cancer Center, Houston, TX, USA*
[6]*Department of Clinical Therapeutics, University of Athens, Athens, Greece*

Abstract

Purpose: Androgen receptor (AR) signaling affects prostate cancer (PCa) growth, metabolism, and progression. Often, PCa progresses from androgen-sensitive to castration-resistant prostate cancer (CRPC) following androgen-deprivation therapy. Clinicopathologic and genomic characterizations of CRPC tumors lead to subdividing CRPC into two subtypes: (1) AR-dependent CRPC containing dysregulation of AR signaling alterations in AR such as amplification, point mutations, and/or generation of splice variants in the *AR* gene; and (2) an aggressive variant PCa (AVPC) subtype that is phenotypically similar to small cell prostate cancer and is defined by chemotherapy sensitivity, gain of neuroendocrine or pro-neural marker expression, loss of AR expression, and combined alterations of PTEN, TP53, and RB1 tumor suppressors. Previously, we reported patient-derived xenograft (PDX) animal models that contain characteristics of these CRPC subtypes. In this study, we have employed the PDX models to test metabolic alterations in the CRPC subtypes.

Procedures: Mass spectrometry and nuclear magnetic resonance analysis along with *in vivo* hyperpolarized 1-[^{13}C]pyruvate spectroscopy experiments were performed on prostate PDX animal models.

Electronic supplementary material The online version of this article (https://doi.org/10.1007/s11307-018-1199-6) contains supplementary material, which is available to authorized users.

Correspondence to: Pratip Bhattacharya; *e-mail:* pkbhattacharya@mdanderson.org

Results: Using hyperpolarized 1-[^{13}C]pyruvate conversion to 1-[^{13}C]lactate *in vivo* as well as lactate measurements *ex vivo*, we have found increased lactate production in AR-dependent CRPC PDX models even under low-hormone levels (castrated mouse) compared to AR-negative AVPC PDX models.
Conclusions: Our analysis underscores the potential of hyperpolarized metabolic imaging in determining the underlying biology and *in vivo* phenotyping of CRPC.

Key words: Hyperpolarized pyruvate, 13C MR, NMR spectroscopy

Introduction

Androgen receptor (AR) signaling regulated by androgen ligands is one of the most critical pathways for prostate cancer (PCa) pathogenesis and progression [1, 2]. Androgen ablation is used as a first-line PCa therapy to inhibit gonadal androgen biosynthesis resulting in inhibition of AR signaling. However, patients often succumb to the disease due to PCa progressing from androgen-sensitive disease to castration-resistant PCa (CRPC) with metastatic progression. Second-generation inhibitors, abiraterone acetate and enzalutamide, target ligand-dependent AR signaling by inhibiting adrenal or intratumoral androgen biosynthesis and blocking AR nuclear translocation, respectively. These second-generation AR signaling inhibitors provide many benefits and increase progression-free survival of PCa patients [3–7].

Molecular analysis of PCa tumors has identified multiple mechanisms that are associated with resistance to the AR inhibition therapy and are associated with heterogeneous clinical subtypes with complex molecular alterations. These mechanisms include alterations in AR such as amplification of the *AR* gene, point mutations in the *AR* gene, and generation of splice variants (*e.g.*, *AR-V7*) that promote development of AR-dependent CRPC disease [2], in which downstream AR signaling can drive disease in the absence or under low androgen conditions and thus, cannot be inhibited by therapy targeting only ligand-dependent AR interaction. A clinically aggressive variant PCa (AVPC) subtype, that is phenotypically similar to small cell prostate cancer, is defined by chemotherapy sensitivity and by gain of neuroendocrine or pro-neural marker expression and loss of AR expression, resulting in the development of AR-independent PCa [1, 8]. Molecular analysis of AVPC demonstrated that combined losses of multiple tumor suppressors including PTEN, TP53, and RB1 are associated with epithelial lineage plasticity leading to development of morphologically heterogeneous PCa subtypes, which are no longer dependent on AR signaling [1, 8–10].

Several studies have shown that AR activation stimulates growth and increases metabolism in PCa [11–14]. AR signaling upregulates expression of multiple glycolytic proteins, such as glucose transporter 1 (GLUT1), hexokinase I and II (HK1 and HK2), and phosphofructokinase (PFK) [11, 15]. In glycolysis, AR induces increased lactate production [11]. Recently, Shafi et al. found that AR splice variant AR-V7 expression also increased lactate production [15]. Using a doxycycline-inducible promoter, they were able to show that increasing the expression of *AR-V7* increased lactate production similarly to androgen in LNCaP cells, indicating that ligand-independent AR signaling also stimulates lactate production in PCa cells.

Since the 1920s, it has been known that cancer cells have increased glycolysis followed by lactic acid production compared to normal cells [16, 17]. This increase is often called "the Warburg effect." Loss of tumor suppressors such as PTEN and TP53 can induce the Warburg effect in PCa cells mediated by HK2 [18]. Clinically, positron-emission tomography (PET) with 2-deoxy-2-[^{18}F]fluoro-D-glucose ([^{18}F]FDG) uptake is often used as a surrogate marker of the Warburg effect. In this regard, [^{18}F]FDG-PET is useful for the diagnosis of a number of cancers in the clinic. However, slow-growing prostate tumors do not show an appreciable difference in [^{18}F]FDG uptake compared to normal or abnormal prostate tissue; therefore, [^{18}F]FDG-PET has poor diagnostic value in local staging of PCa [19]. Furthermore, location of the malignancy in a high background region (bladder) can hinder tumor detection. As such, an alternative metabolic imaging technique is needed that can be utilized where [^{18}F]FDG-PET fails.

Hyperpolarization allows for significant magnetic resonance (MR) signal enhancement, > 10,000-fold compared to Boltzmann polarization, and this enhancement is preserved on the metabolites of the hyperpolarized compound enabling direct observation of metabolic flux [20–22]. Dynamic nuclear polarization (DNP) is often used to polarize small molecules with a majority of research focused on the use of 1-[^{13}C]pyruvate [23, 24]. This molecule is readily taken up by malignant cells and rapidly metabolized to 1-[^{13}C]lactate by lactate dehydrogenase (LDHA) [21, 25–28]. The conversion of hyperpolarized pyruvate can be quantified *in vivo* by measuring the integration of the hyperpolarized lactate signal over the combined hyperpolarized signal from pyruvate and lactate (nLac). nLac is the percentage of hyperpolarized MR signal that originates from lactate, *i.e.*, nLac = lactate/(lactate + pyruvate) [29]. A clinical DNP instrument (SPINLab from GE instruments) is commercially available and the first-in-man study using 1-[^{13}C]pyruvate has been published [28].

The research described herein addresses a key knowledge gap towards linking differential metabolic biochemistry associated with alterations in AR signaling in CRPC into a viable imaging biomarker employing hyperpolarized 1-[^{13}C]pyruvate. To do this, we leveraged previously characterized patient-derived xenografts (PDX) animal models representing AR-dependent CRPC and AR-independent AVPC disease [8, 30, 31]. The AR-expressing PDX models contain castration-resistant AR alterations, such as increased *AR* expression, *AR* mutation, and *AR-V7* expression, indicating typical changes for ligand-independent AR signaling in CRPC tumors. The AR-negative PDX models contain loss of tumor suppressors along with loss of epithelial lineage markers including AR, indicating characteristics of AR-independent AVPC tumors.

Methods

Patient-Derived Xenograft Tumors

Intact or castrated male SCID mice were implanted subcutaneously on the flank with a tumor tissue piece of PDX tumor as previously described [30, 31]. The CRPC and AVPC PDX tumor models were characterized and published [8, 30, 31]. Currently, the xenograft models only can be grown as subcutaneous tumors, but not in the prostate of mice. In addition, these tumor lines cannot be grown as cell lines *via in vitro* culture. Tumors were allowed to grow and all mice were imaged when PDX tumors were approximately 1 to 1.2 cm in diameter. All animal experiments were conducted in accordance with accepted standards of animal care and were approved by the Institutional Animal Care and Use Committee of The University of Texas MD Anderson Cancer Center.

Statistical Analyses

All statistical analyses were performed with GraphPad Prism version 6.00 for Windows, GraphPad Software, La Jolla, CA, USA, www.graphpad.com. *P* values are given for all analyses and statistical significance determined to be any *P* value below 0.05.

Hyperpolarized In Vivo Imaging

Ox063 trityl radical (GE Healthcare, Amersham, Denmark) was mixed with neat 1-[^{13}C]pyruvic acid (Isotech Sigma-Aldrich, St. Louis, MO) to a concentration of 15 mM. Twenty microliters of this solution with 0.4 µl of 50 mM Gd^{3+} (Magnevist, Bayer healthcare, Wayne, NJ) was loaded into a DNP commercial HyperSense polarizer (Oxford Instrument, Abingdon, UK) and irradiated at a microwave frequency of 94.100 GHz for 30–40 min (until polarization plateau) and then dissolved in 4 ml buffer solution containing 40 mM TRIS (7.6 pH preset), 80 mM NaOH, 0.1 g/l EDTA, and 50 mM NaCl. We routinely observe solid state hyperpolarization signal amplitudes around 21,000. After dissolution, neutral (pH 7–8) 80 mM hyperpolarized 1-[^{13}C]pyruvate solution was injected *via* a tail vein catheter.

MRI and MRS were conducted with a ^{1}H volume coil (Bruker BioSpin) with a transmit/receive C-13 surface coil (OD 20 mm, ID15 mm, Doty Scientific Inc., Columbia, SC) placed directly on the tumor in a 7 T Bruker Biospec horizontal bore MR scanner (Bruker BioSpin MRI GmbH, Ettingen, Germany) equipped with a single channel for carbon excitation/reception. Anatomical images were collected using a proton multi-slice T2-weighted RARE sequence. An 8 M [^{13}C]-urea phantom doped with gadolinium-DPTA was placed on top of the surface coil for chemical shift referencing. A series of slice-selective ^{13}C spectra (field-of-view 40×40 mm, slice-thickness 10–12 mm) were collected right after injection of hyperpolarized 1-[^{13}C]pyruvate. The single slice was positioned over the tumor using the multi-slice proton imaging sequence for placement. A total of 90 transients were collected with a time delay between each transient of 2 s (total time 3 min). Each transient used a 15°–20° flip angle excitation pulse (gauss pulse) and 2048 data points. Data were processed in MATLAB (MathWorks Inc., Natick, MA), TopSpin (Bruker BioSpin GmbH, Ettingen, Germany), or MestReNova (Mestrelab Research, Santiago, Spain). Dynamic spectra were manually phased and line-broadening was applied (10 to 15 Hz). The areas under the spectral resonances for pyruvate and lactate were integrated over the whole array. Normalized lactate (nLac) ratios were calculated as lactate over the sum of pyruvate and lactate signals [29, 32].

NMR Metabolism Measurements

For all high-resolution MRS, 1D ^{1}H proton spectroscopy was performed with water suppression on a 500 MHz Bruker Avance III HD NMR equipped with a Prodigy BBO cryoprobe. The cryoprobe increases the sensitivity of the measurement three- to fourfold. All supplies (D_2O, DSS-d_6 (3-trimethylsilyl-1-propanesulfonic acid-d_6 sodium salt), phosphate buffer) were purchased from Sigma-Aldrich without further purification.

Metabolites were extracted with 200 µl of UHPLC grade water (Optima, Thermo Fisher Scientific) from freshly harvested flash-frozen 133-4 and 144-13 PDX tumors from intact mice. Equal aliquots were used for the NMR analysis [33, 34] and steroid mass spectrometry [31]. NMR samples were normalized based on mass using dilution with deuterium oxide. Approximately 21 mg of wet tissue mass was utilized per sample. Each sample contained 0.5 mM DSS-d_6. 1D ^{1}H-NMR spectroscopy was performed on each sample using 256 scans, a spectral width (SW) of 10,245 Hz and referenced to DSS-d_6 at 0.00 ppm. Water suppression was performed with presaturation. Data were processed/analyzed with Chenomx (Chenomx, Inc., Edmonton,

Alberta) and MestreNova (Mestrelab Research, Santiago, Spain). Integrated values of metabolites were determined by taking the ratio of the resonance for each metabolite over the DSS-d_6 peak. Metabolite resonances were identified through reference to either of two online metabolomics databases: Human Metabolome Database (http://www.hmdb.ca) [35] or Biological Magnetic Resonance Bank (http://www.bmrb.wisc.edu/metabolomics). Six individual tumors from each PDX line were utilized.

Metabolites were extracted from freshly harvested flash-frozen tumor tissue from 133-4 PDX grown in intact (133-4) and castrated mice (133-4C). PDX tissue was equally distributed for metabolic analysis using NMR and mass spectrometry. PDX tissue for NMR was homogenized using a liquid nitrogen-cooled mortar and pestle, and then metabolites were extracted with ice-cooled 2:1 methanol to water solution and ~500 µl of MP Biomedicals lysing matrix D beads per 100 mg of tissue. The tissue was further homogenized with three freeze-thaw cycles using liquid nitrogen with a 1-min vortex between each cycle. The homogenates were then centrifuged for 10 min at 4000×*g*, supernatant removed, lyophilized overnight, and the remaining metabolites were dissolved in D_2O with 0.5 mM DSS-d_6, 50 mM K_2HPO_4 (pH 7.4). Approximately 96 mg of wet tissue mass was utilized per sample. Samples were prepared and analyzed in the same manner as those in the previous experiment. Tumor tissue was used from four 133-4C (castrated) mice and three 133-4 (intact) mice.

Mass Spectrometry Analysis

PDX tissues (100 mg) were homogenized in 200 µl UHPLC grade water at 4° using a Bullet Blender and stainless steel beads (3.2 and 1.6 mm diameter, Next Advance, Inc., Averill Park, NY). Samples were centrifuged for 1 min (microcentrifuge at 885×*g*) and 700 µl of UHPLC grade methanol (Optima, Thermo Fisher Scientific) was added. The pellet was homogenized again, centrifuged at 14,167×*g* for 10 min, and the supernatant was transferred to a 5-ml glass test tube. The tissue residue was further extracted twice with 1 ml of 75 % methanol/water. The supernatants were combined, 1.0 ng ^{3}d-malic acid (CDN Isotopes, Point Claire, Canada) was added, and samples were dried under nitrogen at room temperature. The samples were reconstituted in 100 µl of 75 % methanol/water and derivatized to the 3-nitrophenylhydrozones as described by Han et al. [36]. Chromatographic separation of derivatized tricarboxylic acids, fumarate, succinate, malate, and lactate, was conducted using ultra high-pressure liquid chromatography (Agilent 1290 Infinity II, Santa Clara, CA), Chromolith C18 reverse phase column (100 × 2 mm, 1.5 µm) and a mobile phase gradient from 30 % methanol–water with 0.1 % formic acid to 95 % methanol–water with 0.1 % formic acid. Derivatized carboxylic compounds were introduced into the electrospray ion source (Jet Stream, Agilent) and analyzed in the positive ion mode. An Agilent 6495 triple quadrupole mass spectrometer with MassHunter Workstation software (Agilent) was used to quantify analytes. We used the two most sensitive multiple reaction monitoring transitions for each analyte to quantify and verify analyte identity. Parent and product ion transitions for quantitation were *m/z* 403.3 to 137.0 (malate), *m/z* 406.3 to 140.0 (malate-d_3, CDN Isotopes, Pointe-Claire, Quebec, Canada), *m/z* 385.3 to 152.1 (fumarate), *m/z* 387.3 to 152.1 (succinate), and *m/z* 224.2 to 137.1 (lactate). All tricarboxylic acid standards were purchased from Sigma (St. Louis, IL). Testosterone was quantified as described previously [31].

Results

To examine the pyruvate-to-lactate transition in AR-expressing and AR-negative PCa PDXs, we measured the conversion of hyperpolarized 1-[^{13}C]pyruvate to 1-[^{13}C]lactate using slice-selective magnetic resonance spectroscopy (MRS). Two CRPC AR-positive and two AVPC AR-null PDX subtypes (Table 1) that represent local high-risk PCa (model ID180-30), metastatic CRPC to bone (model ID 133-4), and AVPC (model ID 155-2 and model ID144-13) were grown in intact mice as models of PCa preceding androgen deprivation therapy [8, 30, 31]. Both AR-positive PDXs express high levels of AR and AR-V7 under castrate conditions in mice ([31], data not shown for 180-30). In cancer cells, pyruvate is imported quickly by monocarboxylate transporters (MCTs) and converted by lactate dehydrogenase (LDH) in the cytosol to lactate or is converted to acetyl-CoA in the mitochondria and utilized in the citric acid cycle. Due to the low natural abundance and low gyromagnetic ratio for carbon-13, there is no detectable carbon-13 background signal. Therefore, the ratio of hyperpolarized 1-[^{13}C] lactate signal over pyruvate hyperpolarized carbon-13 signal is a measure of pyruvate and lactate transport in tissue [37, 38], conversion of pyruvate into lactate through LDH activity [21, 24], and NADH/NAD+ levels [39, 40] (Fig. 1a).

Slice-selective MRS was used to measure the conversion of hyperpolarized pyruvate in subcutaneous PDX tumors. A MRI axial cross-sectional image of a 180-30 PDX tumor (Fig. 2a) illustrates the placement of the single-slice ^{13}C-spectroscopy sequence to acquire single transient spectra every 2 s over a 3-min period. The right panel of Fig. 2c is the full spectrum array for a 180-30 PDX animal, and representative single transients taken 20 s after injection from each PDX model are depicted in the right panel. The signal value is determined by integrating the resonance for pyruvate at 173 ppm and lactate at 185 ppm for each FID and plotting these values over time (Fig. 2d). The hyperpolarized lactate pool produced in each experiment (nLac) is determined by calculating the area under the time course curve of ^{13}C signal for lactate over the combined ^{13}C signal for lactate and pyruvate (Fig. 2b, d). We have calculated both nLac and the lactate/pyruvate values (Table 1, Supplemental Table); however, it has been shown in phantom

Table 1. Patient-derived xenograft (PDX) models. Table summarizes the PDX models used in this study, the CRPC phenotype of each model, the number of animals utilized, and the average ± standard error of the nLac value. Average nLac values are calculated as a ratio of the hyperpolarized lactate signal over the total hyperpolarized signal from lactate and pyruvate measured using MRI. PDX androgen receptor status is androgen receptor positive (AR+) or androgen receptor negative (AR−). PDX models were grown in the presence of circulating testicular androgen (intact) and without circulating androgen (castrated). References describe each PDX phenotype. All MDA-PCa- defined PDX nomenclature will be identified as short model ID name 180-30, 133-4, 133-4C, 155-2 and 144-13 in text.

PDX model ID	AR status	Number of animals	nLac	Intact/castrated mouse	PCa phenotype with references
MDA-PCa-180-30	AR+	5	0.26 ± 0.06	Intact	Adenocarcinoma; Gleason 9 primary; AR-dependent [31]
MDA-PCa-133-4	AR+	7	0.16 ± 0.03	Intact	Adenocarcinoma; CRPC bone metastasis; AR-dependent [30]
MDA-PCa-133-4C	AR+	7	0.24 ± 0.06	Castrated	Adenocarcinoma; CRPC bone metastasis; AR-dependent [30]
MDA-PCa-155-2	AR−	5	0.11 ± 0.03	Intact	Small cell prostate carcinoma; AVPC primary; AR-independent [8]
MDA-PCa-144-13	AR−	5	0.12 ± 0.06	Intact	Small cell prostate carcinoma; AVPC primary; AR-independent [8]

experiments that standard deviation and coefficient of variation are reduced using nLac *versus* the lactate/pyruvate ratio [41]. In addition, we have determined if the size of the tumor measured by ^{1}H MRI affects the overall conversion values (Supplemental Table). We observe no statistical significance in nLac or lactate/pyruvate values based on tumor size (one-way ANOVA and Tukey multiple comparisons). Average nLac values showed a trend towards increased lactate biosynthesis in AR-expressing *versus* AR-negative PDXs (Table 1). nLac values in AR-positive tumors from intact and castrated mice were greater than 0.15, but both AR-negative tumors were below 0.15 (Table 1). However, statistical significance was only demonstrated when nLac measurements were compared between AR-positive and AR-negative groups (Fig. 1b; $P < 0.04$, unpaired Student's two-tailed t test with Welch correction).

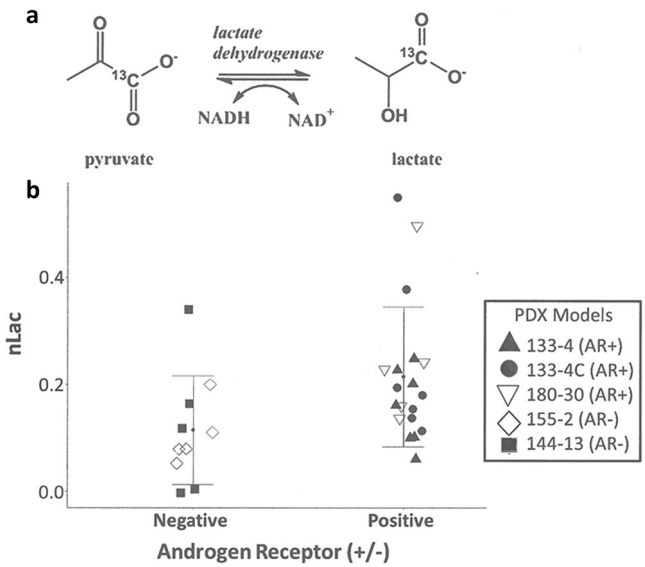

Fig. 1 Metabolic alterations between AR-dependent and AR-independent CRPC. **a** The enzymatic reaction of lactate dehydrogenase which is being interrogated with hyperpolarized 1-[^{13}C]pyruvate. **b** Box plot with all nLac values subdivided into AR(+) and AR(–) values. P value < 0.04 determined using unpaired Student's two-tailed t test with Welch correction.

To further confirm our *in vivo* glycolytic measurements, nuclear magnetic resonance (NMR) and mass spectrometry (MS) were used to measure glycolytic and citric acid cycle metabolites such as lactate, fumarate, and succinate in homogenized tumor tissue samples. We found distinct decreases in lactate and succinate levels both by NMR and MS analysis in 144-13 PDX samples relative to 133-4 samples (Fig. 3a, b). Differences in levels of succinate and lactate measured by MS matched the corresponding levels measured by NMR. These measured lactate levels support the observed difference in pyruvate-to-lactate conversion in hyperpolarized MR of these two PDX models.

The AR signaling axis in the defined CRPC subtypes is demonstrated by measurement of intratumoral testosterone levels (Fig. 3c) and significant nuclear AR expression by immunohistochemistry (Fig. 3d). The testosterone levels in 133-4 and 144-13 PDX tumor samples are similar, but as expected, nuclear AR was detected in 133-4C but not in 144-13 PDX tumors. The testosterone epimer, epitestosterone, was measured to access species-specific interconversion testosterone to epitestosterone and accumulation in PDX tumors [32]. To evaluate the alterations in glycolytic and citric acid cycle metabolites after androgen deprivation therapy, the 133-4 PDX was grown in intact and castrated mice as previously described [31]. Notably, the levels of lactate, succinate, and fumarate were similar in tissue from both castrated and intact mice when measured by NMR and MS, suggesting increases in glycolysis and lactate levels in AR-dependent CRPC is not dependent on androgen levels but is directly driven by AR signaling (Fig. 4a, b).

Discussion

Using preclinical animal models that represent the heterogeneity of CRPC, we found increased glycolysis in AR-positive compared to AR-negative PDX models. These differences were found in overall lactate values *ex vivo* found both by NMR and mass spectral analysis and in real-time flux measurements (nLac) *in vivo*. Lower nLac values found in AVPC AR-negative PDX models indicate that the Warburg effect is less prominent in this lethal variant PCa, suggesting a possibility that lineage plasticity

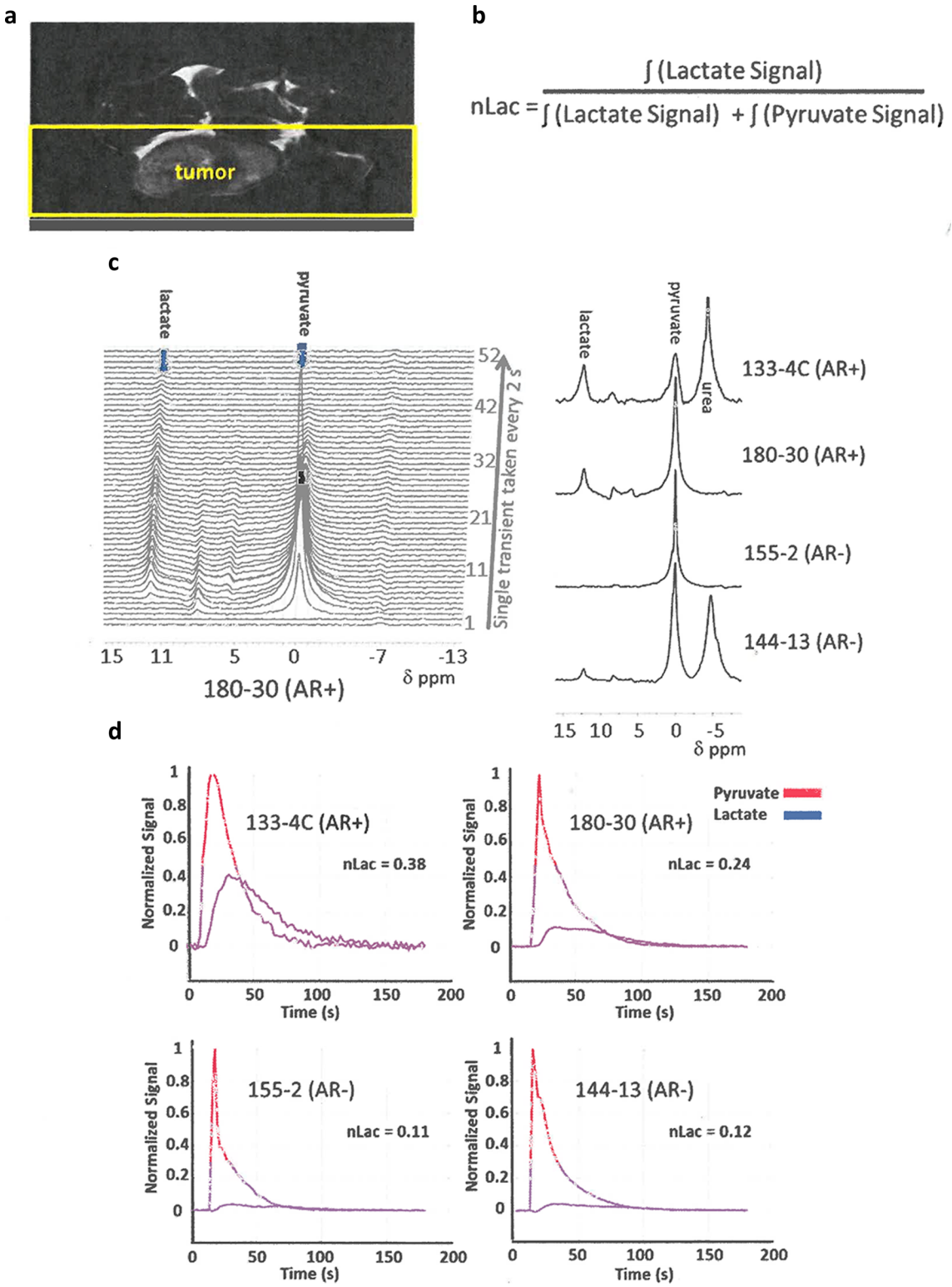

Fig. 2 Hyperpolarized pyruvate to lactate data for PCa PDX models. **a** A representative axial image of a mouse with a subcutaneous PDX CRPC tumor. A series of slice-selective C-13 spectra (field-of-view 40 × 40 mm, slice thickness 10–12 mm) were collected right after injection of hyperpolarized 1-[^{13}C] pyruvate. The single slice (yellow box) was placed over the tumor using the multi-slice proton imaging sequence for placement. **b** nLac is determined by integrating the C-13 signal for lactate over the combined C-13 signal for lactate and pyruvate. **c** Representative array of single spectrum obtained from a 180-30 mouse (left). A single transient was taken every 2 s for a total time of 3 min. Representative single transients taken 20 s after the start of the injection in different PDX animal models (right). **d** The dynamic curves for the same spectroscopy experiments shown in the single traces are shown. Pyruvate signal is in red and lactate signal is in blue.

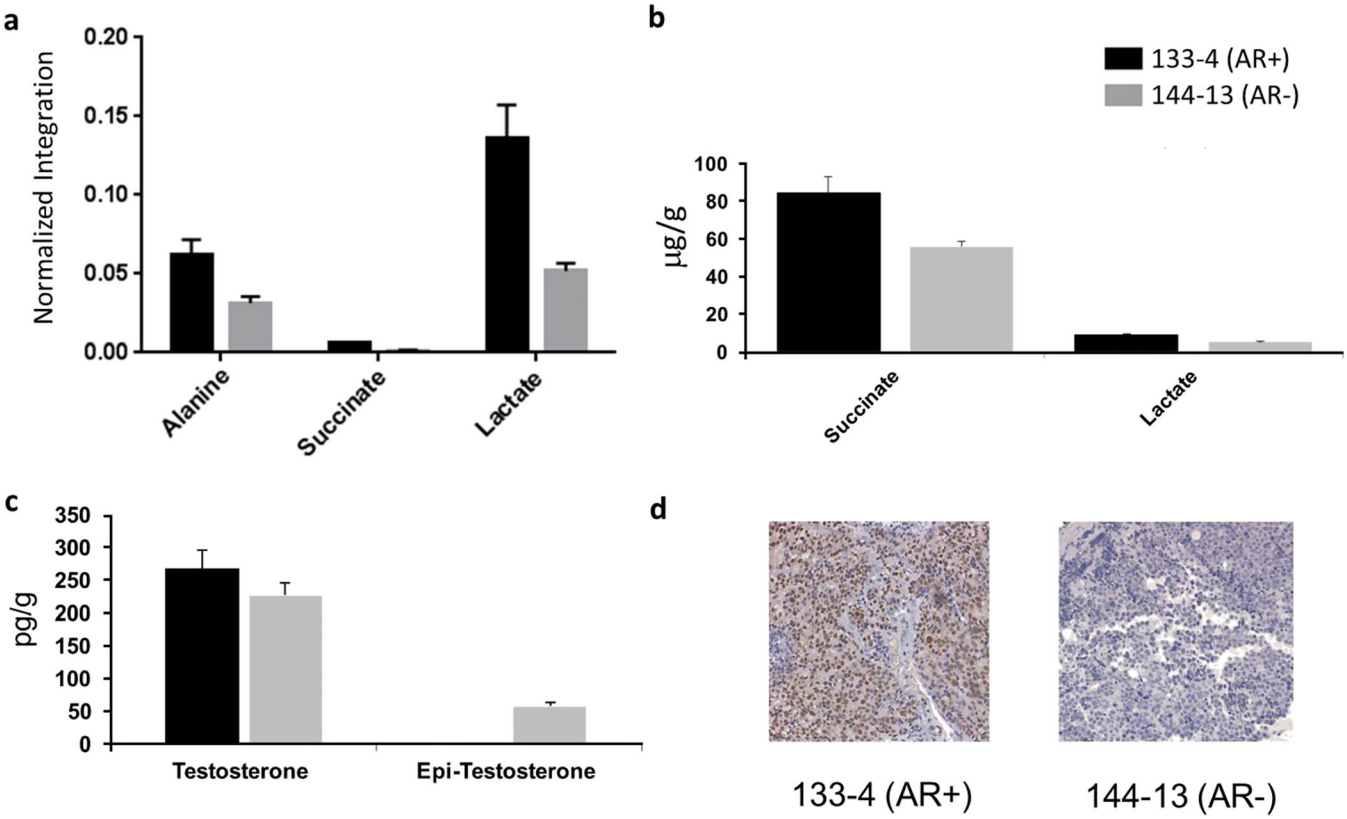

Fig. 3 Glycolytic metabolites in 133-4 and 144-13 models grown in intact mice found by NMR and MS analysis. **a** Graph of NMR measured glycolytic metabolites normalized to wet mass of tissue. Six tumor tissues per PDX model were utilized. Unpaired *t* test using Holm-Sidak method was used to determine statistical significance. Higher amounts of lactate, alanine, and succinate were found in 133-4 tissue *versus* 144-13, $P < 0.02$. **b** Graph for the microgram per gram values of succinate ($P < 0.03$) and lactate ($P < 0.02$) measured by UPLC/MSMS (Mann-Whitney non-parametric analysis). **c** Graph of picogram per gram values of testosterone ($P > 0.05$) and epitestosterone ($P < 0.01$) measured by UPLC/MSMS. The same extracted sample was utilized in the NMR and LC/MSMS assays. **d** Representative immunohistochemical staining of the androgen receptor in 133-4 and 144-13 tumor tissues.

associated with AVPC might allow more utilization of mitochondrial energy metabolism.

Slice-selective MRS was used to measure the conversion of hyperpolarized pyruvate in subcutaneous PDX tumors, although for imaging in the prostate, other more dynamic spatial sequences [42–44] will be required and could increase the overall sensitivity of the assay. Normal tissue is often less glycolytic than malignant tissue and has much lower expression

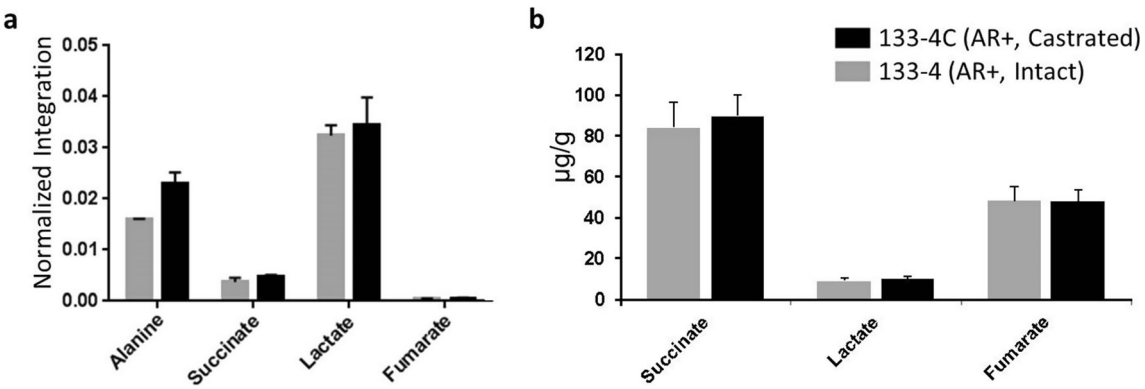

Fig. 4 Glycolytic metabolites in 133-4 model in castrated and intact mice found by NMR and MS analysis. **a** Graph of metabolites measured using NMR normalized to wet mass of tissue in 133-4 PDX model grown both in intact male mice and castrated male mice. **b** Microgram per gram of succinate, lactate, and fumarate measured using UPLC-MS/MS. Levels of all three metabolites were observed to be quite similar in both tissue types (castrated 133-4C tissue, $n = 4$; intact 133-4 tissue, $n = 3$).

of MCTs [45] compared to cancer cells which reduces the uptake of hyperpolarized pyruvate. Zierhut et al. observed low pyruvate to lactate conversion in normal mice within most tissue [46] and low pyruvate to lactate conversion is observed in normal prostate tissue in patients [28]. As can be observed in Fig. 2a, depending on the size of the tumor, some normal tissue could be in our slice-selective MRS used to measure the conversion of hyperpolarized pyruvate that could possibly affect our overall values. Nonetheless, our analysis underscores the potential hyperpolarized metabolic imaging has for determining the underlying biology in a PCa and *in vivo* phenotyping CRPC into AVPC or AR-dependent disease.

With the advances in second-generation AR inhibition compounds (abiraterone acetate and enzalutamide), a non-invasive *in vivo* method to determine if AR signaling is intact even when a patient has undetectable blood androgen levels would help determine if these new agents should be used in a specific patient for neoadjuvant or adjuvant therapy. We are in the process of determining how hyperpolarized pyruvate-to-lactate conversion (nLac) changes in animals treated with abiraterone acetate and enzalutamide. If the dysregulation of *AR* drives directly the increase in glycolytic flux of lactate dehydrogenase in AR-dependent CRPC, our hypothesis is with complete shutdown of AR signaling in an AR-dependent CRPC, one would observe a reduction in nLac after treatment compared to a pretreatment measurement and could be used as a marker of therapy response.

Conclusions

Employing mass spectrometry and nuclear magnetic resonance analysis along with *in vivo* hyperpolarized 1-[^{13}C]pyruvate spectroscopy experiments on prostate PDX animal models, we have demonstrated the potential of metabolic imaging in determining the underlying biology and *in vivo* phenotyping of castration-resistant prostate cancer. Future studies will focus on interrogating the efficacy of enhanced androgen signaling inhibition therapy in these mouse models as well as translating these techniques to future clinic trials. It is likely that metabolomics and hyperpolarized metabolic imaging is the next frontier in prostate cancer diagnosis and assessing therapeutic efficacy; with the combined knowledge of genomics and proteomics, a complete understanding of tumorigenesis in prostate might be achieved.

Funding Information The research was funded in part by a grant from the U.S. Department of Defense (CDMRP PC110065, NZ, SS, JL); by Institutional Research Grants (NMZ, PB); Koch Foundation Genitourinary Medical Oncology Funds (NZ, PB, MT, SM, DPW) and a startup grant (PB) from MD Anderson Cancer Center; by grants from the U.S. National Cancer Institute (P50 CA 094056, U54 CA151668, R21CA185536); and by a grant from the Gulf Coast Consortium (JL, PB). This work also was supported by the National Institutes of Health/NCI Cancer Center Support Grant under award number P30CA016672, Prostate Cancer Patient Derived Xenografts Program Core and used the small animal imaging and the NMR spectroscopy core facilities at MD Anderson Cancer Center.

Compliance with Ethical Standards

Conflict of Interest

The authors declare that they have no conflict of interest.

References

1. Logothetis CJ, Gallick GE, Maity SN, Kim J, Aparicio A, Efstathiou E, Lin SH (2013) Molecular classification of prostate cancer progression: foundation for marker-driven treatment of prostate cancer. Cancer Discov 3:849–861
2. Yuan X, Cai C, Chen S, Chen S, Yu Z, Balk SP (2014) Androgen receptor functions in castration-resistant prostate cancer and mechanisms of resistance to new agents targeting the androgen axis. Oncogene 33:2815–2825
3. de Bono JS, Logothetis CJ, Molina A, Fizazi K, North S, Chu L, Chi KN, Jones RJ, Goodman OB Jr, Saad F, Staffurth JN, Mainwaring P, Harland S, Flaig TW, Hutson TE, Cheng T, Patterson H, Hainsworth JD, Ryan CJ, Sternberg CN, Ellard SL, Fléchon A, Saleh M, Scholz M, Efstathiou E, Zivi A, Bianchini D, Loriot Y, Chieffo N, Kheoh T, Haqq CM, Scher HI, COU-AA-301 Investigators (2011) Abiraterone and increased survival in metastatic prostate cancer. N Engl J Med 364:1995–2005
4. Ryan CJ, Shah S, Efstathiou E, Smith MR, Taplin ME, Bubley GJ, Logothetis CJ, Kheoh T, Kilian C, Haqq CM, Molina A, Small EJ (2011) Phase II study of abiraterone acetate in chemotherapy-naive metastatic castration-resistant prostate cancer displaying bone flare discordant with serologic response. Clin Cancer Res 17:4854–4861
5. Efstathiou E, Titus M, Tsavachidou D, Tzelepi V, Wen S, Hoang A, Molina A, Chieffo N, Smith LA, Karlou M, Troncoso P, Logothetis CJ (2012) Effects of abiraterone acetate on androgen signaling in castrate-resistant prostate cancer in bone. J Clin Oncol 30:637–643
6. Cookson MS, Roth BJ, Dahm P, Engstrom C, Freedland SJ, Hussain M, Lin DW, Lowrance WT, Murad MH, Oh WK, Penson DF, Kibel AS (2013) Castration-resistant prostate cancer: AUA Guideline. J Urol 190:429–438
7. Chen EJ, Sowalsky AG, Gao S, Cai C, Voznesensky O, Schaefer R, Loda M, True LD, Ye H, Troncoso P, Lis RL, Kantoff PW, Montgomery RB, Nelson PS, Bubley GJ, Balk SP, Taplin ME (2015) Abiraterone treatment in castration-resistant prostate cancer selects for progesterone responsive mutant androgen receptors. Clin Cancer Res 21:1273–1280
8. Aparicio AM, Shen L, Tapia EL, Lu JF, Chen HC, Zhang J, Wu G, Wang X, Troncoso P, Corn P, Thompson TC, Broom B, Baggerly K, Maity SN, Logothetis CJ (2016) Combined tumor suppressor defects characterize clinically defined aggressive variant prostate cancers. Clin Cancer Res 22:1520–30
9. Ku SY, Rosario S, Wang Y, Mu P, Seshadri M, Goodrich ZW, Goodrich MM, Labbé DP, Gomez EC, Wang J, Long HW, Xu B, Brown M, Loda M, Sawyers CL, Ellis L, Goodrich DW (2017) Rb1 and Trp53 cooperate to suppress prostate cancer lineage plasticity, metastasis, and antiandrogen resistance. Science 355:78–83
10. Mu P, Zhang Z, Benelli M, Karthaus WR, Hoover E, Chen CC, Wongvipat J, Ku SY, Gao D, Cao Z, Shah N, Adams EJ, Abida W, Watson PA, Prandi D, Huang CH, de Stanchina E, Lowe SW, Ellis L, Beltran H, Rubin MA, Goodrich DW, Demichelis F, Sawyers CL (2017) SOX2 promotes lineage plasticity and antiandrogen resistance in TP53- and RB1-deficient prostate cancer. Science 355:84–88
11. Massie CE, Lynch A, Ramos-Montoya A, Boren J, Stark R, Fazli L, Warren A, Scott H, Madhu B, Sharma N, Bon H, Zecchini V, Smith DM, DeNicola GM, Mathews N, Osborne M, Hadfield J, MacArthur S, Adryan B, Lyons SK, Brindle KM, Griffiths J, Gleave ME, Rennie PS, Neal DE, Mills IG (2011) The androgen receptor fuels prostate cancer by regulating central metabolism and biosynthesis. EMBO J 30:2719–2733
12. Tennakoon JB, Shi Y, Han JJ, Tsouko E, White MA, Burns AR, Zhang A, Xia X, Ilkayeva OR, Xin L, Ittmann MM, Rick FG, Schally AV, Frigo DE (2014) Androgens regulate prostate cancer cell growth

via an AMPK-PGC-1alpha-mediated metabolic switch. Oncogene 33:5251–5261
13. Tsouko E, Khan AS, White MA, Han JJ, Shi Y, Merchant FA, Sharpe MA, Xin L, Frigo DE (2014) Regulation of the pentose phosphate pathway by an androgen receptor-mTOR-mediated mechanism and its role in prostate cancer cell growth. Oncogene 3:e103
14. White MA, Lin C, Rajapakshe K, Dong J, Shi Y, Tsouko E, Mukhopadhyay R, Jasso D, Dawood W, Coarfa C, Frigo DE (2017) Glutamine transporters are targets of multiple oncogenic signaling pathways in prostate cancer. Mol Cancer Res 15:1017–1028
15. Shafi AA, Putluri V, Arnold JM, Tsouko E, Maity S, Roberts JM, Coarfa C, Frigo DE, Putluri N, Sreekumar A, Weigel NL (2015) Differential regulation of metabolic pathways by androgen receptor (AR) and its constitutively active splice variant, AR-V7, in prostate cancer cells. Oncotarget 6:31997–32012
16. Warburg O (1956) On the origin of cancer cells. Science 123:309–314
17. Warburg O (1956) On respiratory impairment in cancer cells. Science 124:269–270
18. Wang L, Xiong H, Wu F, Zhang Y, Wang J, Zhao L, Guo X, Chang LJ, Zhang Y, You MJ, Koochekpour S, Saleem M, Huang H, Lu J, Deng Y (2014) Hexokinase 2-mediated Warburg effect is required for PTEN- and p53-deficiency-driven prostate cancer growth. Cell Rep 8:1461–1474
19. Wibmer AG, Burger IA, Sala E, Hricak H, Weber WA, Vargas HA (2016) Molecular imaging of prostate cancer. Radiographics 36:142–159
20. Golman K, Zandt RI, Lerche M et al (2006) Metabolic imaging by hyperpolarized ^{13}C magnetic resonance imaging for in vivo tumor diagnosis. Cancer Res 66:10855–10860
21. Albers MJ, Bok R, Chen AP, Cunningham CH, Zierhut ML, Zhang VY, Kohler SJ, Tropp J, Hurd RE, Yen YF, Nelson SJ, Vigneron DB, Kurhanewicz J (2008) Hyperpolarized ^{13}C lactate, pyruvate, and alanine: noninvasive biomarkers for prostate cancer detection and grading. Cancer Res 68:8607–8615
22. Brindle KM, Bohndiek SE, Gallagher FA, Kettunen MI (2011) Tumor imaging using hyperpolarized ^{13}C magnetic resonance spectroscopy. Magn Reson Med 66:505–519
23. Brindle K (2008) New approaches for imaging tumour responses to treatment. Nat Rev Cancer 8:94–107
24. Kurhanewicz J, Vigneron DB, Brindle K, Chekmenev EY, Comment A, Cunningham CH, DeBerardinis RJ, Green GG, Leach MO, Rajan SS, Rizi RR, Ross BD, Warren WS, Malloy CR (2011) Analysis of cancer metabolism by imaging hyperpolarized nuclei: prospects for translation to clinical research. Neoplasia 13:81–97
25. Chen AP, Albers MJ, Cunningham CH, Kohler SJ, Yen YF, Hurd RE, Tropp J, Bok R, Pauly JM, Nelson SJ, Kurhanewicz J, Vigneron DB (2007) Hyperpolarized C-13 spectroscopic imaging of the TRAMP mouse at 3T-initial experience. Magn Reson Med 58:1099–1106
26. Golman K, in 't Zandt R, Thaning M (2006) Real-time metabolic imaging. Proc Natl Acad Sci U S A 103:11270–11275
27. Hurd RE, Yen YF, Chen A, Ardenkjaer-Larsen JH (2012) Hyperpolarized ^{13}C metabolic imaging using dissolution dynamic nuclear polarization. J Magn Reson Imaging 36:1314–1328
28. Nelson SJ, Kurhanewicz J, Vigneron DB et al (2013) Metabolic imaging of patients with prostate cancer using hyperpolarized [1-^{13}?C]pyruvate. Sci Transl Med 5:198ra108
29. Benito J, Ramirez MS, Millward NZ, Velez J, Harutyunyan KG, Lu H, Shi YX, Matre P, Jacamo R, Ma H, Konoplev S, McQueen T, Volgin A, Protopopova M, Mu H, Lee J, Bhattacharya PK, Marszalek JR, Davis RE, Bankson JA, Cortes JE, Hart CP, Andreeff M, Konopleva M (2016) Hypoxia-activated prodrug TH-302 targets hypoxic bone marrow niches in preclinical leukemia models. Clin Cancer Res 22:1687–1698
30. Tzelepi V, Zhang J, Lu JF, Kleb B, Wu G, Wan X, Hoang A, Efstathiou E, Sircar K, Navone NM, Troncoso P, Liang S, Logothetis CJ, Maity SN, Aparicio AM (2012) Modeling a lethal prostate cancer variant with small-cell carcinoma features. Clin Cancer Res 18:666–677
31. Maity SN, Titus MA, Gyftaki R, Wu G, Lu JF, Ramachandran S, Li-Ning-Tapia EM, Logothetis CJ, Araujo JC, Efstathiou E (2016) Targeting of CYP17A1 lyase by VT-464 inhibits adrenal and intratumoral androgen biosynthesis and tumor growth of castration resistant prostate cancer. Sci Rep 6:35354
32. Lee J, Ramirez MS, Walker CM, Chen Y, Yi S, Sandulache VC, Lai SY, Bankson JA (2015) High-throughput hyperpolarized ^{13}C metabolic investigations using a multi-channel acquisition system. J Magn Reson 260:20–27
33. Ornelas A, McCullough CR, Lu Z, Zacharias NM, Kelderhouse LE, Gray J, Yang H, Engel BJ, Wang Y, Mao W, Sutton MN, Bhattacharya PK, Bast RC, Millward SW (2016) Induction of autophagy by ARHI (DIRAS3) alters fundamental metabolic pathways in ovarian cancer models. BMC Cancer 16:824
34. Zacharias NM, McCullough C, Shanmugavelandy S, Lee J, Lee Y, Dutta P, McHenry J, Nguyen L, Norton W, Jones LW, Bhattacharya PK (2017) Metabolic differences in glutamine utilization lead to metabolic vulnerabilities in prostate cancer. Sci Rep 7:16159
35. Wishart DS, Jewison T, Guo AC, Wilson M, Knox C, Liu Y, Djoumbou Y, Mandal R, Aziat F, Dong E, Bouatra S, Sinelnikov I, Arndt D, Xia J, Liu P, Yallou F, Bjorndahl T, Perez-Pineiro R, Eisner R, Allen F, Neveu V, Greiner R, Scalbert A (2013) HMDB 3.0—the Human Metabolome Database in 2013. Nucleic Acids Res 41:D801–D807
36. Han J, Gagnon S, Eckle T, Borchers CH (2013) Metabolomic analysis of key central carbon metabolism carboxylic acids as their 3-nitrophenylhydrazones by UPLC/ESI-MS. Electrophoresis 34:2891–2900
37. Viswanath P, Najac C, Izquierdo-Garcia JL, Pankov A, Hong C, Eriksson P, Costello JF, Pieper RO, Ronen SM (2016) Mutant IDH1 expression is associated with down-regulation of monocarboxylate transporters. Oncotarget 7:34942–34955
38. Balzan R, Fernandes L, Pidial L, Comment A, Tavitian B, Vasos PR (2017) Pyruvate cellular uptake and enzymatic conversion probed by dissolution DNP-NMR: the impact of overexpressed membrane transporters. Magn Reson Chem 55:579–583
39. Hurd RE, Spielman D, Josan S, Yen YF, Pfefferbaum A, Mayer D (2013) Exchange-linked dissolution agents in dissolution-DNP ^{13}C metabolic imaging. Magn Reson Med 70:936–942
40. Sandulache VC, Chen Y, Lee J, Rubinstein A, Ramirez MS, Skinner HD, Walker CM, Williams MD, Tailor R, Court LE, Bankson JA, Lai SY (2014) Evaluation of hyperpolarized [1-(1)(3)C]-pyruvate by magnetic resonance to detect ionizing radiation effects in real time. PLoS One 9:e87031
41. Walker CM, Lee J, Ramirez MS, Schellingerhout D, Millward S, Bankson JA (2013) A catalyzing phantom for reproducible dynamic conversion of hyperpolarized [1-^{13}?C]-pyruvate. PLoS One 8:e71274
42. Gordon JW, Larson PE (2016) Pulse sequences for hyperpolarized MRS. EMAGRES 5:1229–1245
43. Park, J. M., Josan, S., Jang, T., Merchant M., Watkins R., Hurd R. E., Recht L. D., Mayer D., Spielman D. M. (2016) Volumetric spiral chemical shift imaging of hyperpolarized [2-[^{13}? C]pyruvate in a rat c6 glioma model. Magn Reson Med 75: 973–984
44. Gordon JW, Vigneron DB, Larson PE (2017) Development of a symmetric echo planar imaging framework for clinical translation of rapid dynamic hyperpolarized ^{13}C imaging. Magn Reson Med 77:826–832
45. Perez-Escuredo J, Van Hee VF, Sboarina M et al (2016) Monocarboxylate transporters in the brain and in cancer. Biochim Biophys Acta 1863:2481–2497
46. Zierhut ML, Yen YF, Chen AP, Bok R, Albers MJ, Zhang V, Tropp J, Park I, Vigneron DB, Kurhanewicz J, Hurd RE, Nelson SJ (2010) Kinetic modeling of hyperpolarized ^{13}C1-pyruvate metabolism in normal rats and TRAMP mice. J Magn Reson 202:85–92